CrystEngComm

PAPER

View Article Online
View Journal | View Issue

Cite this: *CrystEngComm*, 2018, **20**, 4666

Synthesis of hydrophobic MIL-53(Al) nanoparticles in low molecular weight alcohols: systematic investigation of solvent effects†

Jan Warfsmann, [a] Begum Tokay *[a] and Neil R. Champness *[b]

Received 1st June 2018,
Accepted 5th July 2018

DOI: 10.1039/c8ce00913a

rsc.li/crystengcomm

The effects of using low molecular weight alcohols, methanol (MeOH) and ethanol (EtOH), for the synthesis of MIL-53(Al) are investigated and the results are directly compared with analogous synthesis in water and *N*,*N*-dimethylformamide (DMF). We have successfully synthesised MIL-53(Al), termed MIL-53(MeOH), using MeOH as the solvent and employing a reaction temperature of 150 °C, lower than that typically used for analogous water or DMF-based reactions. Several unique properties are observed for MIL-53(MeOH). The breathing phenomenon which is known for MIL-53(Al) derivatives, prepared using water or DMF as the reaction solvent, is not observed for samples prepared from MeOH and the framework adopts and remains in the large-pore form. Thus, measurement of N_2-isotherms and calculation of internal surface areas have verified that the synthesis of MIL-53(MeOH) leads to a product which is highly porous with only minimal or no activation required. Furthermore, X-ray diffraction measurements and scanning electron microscopy at different humidity levels reveal a reversible loss of crystallinity at high humidity levels for MIL-53(MeOH) which was not observed previously for other MIL-53 derivatives. In contrast, the synthesis of MIL-53(Al) in ethanol leads to a product with low crystallinity.

Introduction

Metal–organic frameworks (MOFs) have received extensive interest due to their highly porous structure and their ability to act as efficient hosts for guest molecules. The possibility to tune their pore dimensions and functionality has led to the application of MOFs[1] in fields as diverse as gas adsorption,[2] drug delivery,[3] and protein encapsulation,[4] as crystal sponges[5] or in magnetic and electronic devices.[6,7] The MIL-53 class (MIL = Matériaux de l'Institut Lavoisier) of materials has received much attention due to their unusual structural behaviour. Férey *et al.* reported the first chromium-containing MIL-53,[8] formed by $CrO_4(OH_2)$ octahedral clusters connected by 1,4-benzenedicarboxylate (BDC^{2-}) leading to a porous material with one-dimensional rhombus-shaped channels. The MIL-53 framework can been tuned whilst preserving the overall structure by using different metal sources, *e.g.* Fe,[9,10] Al,[11] Ga[12] and Sc,[13] and/or BDC^{2-} derivatives, *e.g.* amino,[14] fluorine,[15] chlorine, nitro, hydroxyl[16] or carbamate.[17] The possibility to employ post-synthetic modification[18] and using mixtures of metals[19] or ligands[20] in the same framework further increase the variability of MIL-53. As a result, MIL-53 has been successfully applied in gas separation[21] and storage,[22] heavy metal capture,[23] catalysis[24,25] controlled drug delivery,[26] sensing[27] and water treatment.[28] Besides its structural variability, MIL-53 is particularly notable for the so-called breathing effect.[11,29] MIL-53 has a flexible framework and the internal pore size and volume change by up to 33%[12,30] upon appropriate stimulation including guest molecule adsorption[11] or temperature variation.[19] For the aluminium and chromium derivatives, small and large pore forms[11,18] are observed (pore apertures are 0.26 nm × 1.36 nm and 0.85 nm × 0.85 nm, respectively), while for the Fe[31] and Ga[12] derivatives, several additional pore forms exist. The breathing effect of MIL-53 is most commonly caused by adsorption of water or CO_2 and MIL-53 adsorbs water from ambient air within minutes even at a low relative humidity of 10%.[11,32,33] Although the adsorption of water is desired for some applications *e.g.* water capture under ambient conditions for usage as drinking water[34] or in heat pumps,[35] this feature can limit the use of MIL-53 for many industrial applications where adsorbed water has to be removed prior to further application. Due to the ubiquity of humidity in ambient air, several studies have investigated the usage of additional agents or synthesis methods in order to increase the hydrophobicity of MIL-53, such as using ionic liquids[33] or hydrophobic linkers[36] during synthesis. However, possible trade-offs are increased

[a] *Chemical and Environmental Engineering Department, Faculty of Engineering, University of Nottingham, University Park, Nottingham NG7 2RD, UK. E-mail: Begum.Tokay@nottingham.ac.uk*
[b] *School of Chemistry, University Park, University of Nottingham, Nottingham, NG7 2RD, UK. E-mail: Neil.Champness@nottingham.ac.uk*

† Electronic supplementary information (ESI) available. See DOI: 10.1039/c8ce00913a

synthesis times (up to one week) or a reduced pore volume. Although MIL-53 has been synthesized by microwave radiation,[37] ultrasonication[38] or under continuous flow conditions,[39] solvothermal synthesis at autogenous pressure and elevated temperature still remains the most common method to prepare MIL-53, employing *N*,*N*-dimethylformamide (DMF) and water as solvents.[40] Synthesis of MIL-53 in DMF has the advantages of high product yields (up to 100%) and the possible synthesis of nano-sized particles (<100 nm crystals), but DMF is flammable, toxic and can cause congenital disorders.[41] Moreover, low DMF vapour pressure prevents the easy removal of excess/residual DMF (at 20 °C, 0.377 kPa for DMF in comparison with 2.33 kPa for water and 12.9 kPa for MeOH[42]) from the pores and for several MOFs, including MIL-53, coordination of DMF to the MOF metal nodes has been observed, which further complicates the purification/activation process.[43] Therefore, DMF usage in industrial scale synthesis is not recommended and alternatives should be sought.[44] Water would be a suitable alternative solvent, but low yields remain a significant challenge.[45] Another challenge is the difficulty to prepare nano-sized particles in water, which is desirable for use as catalysts, electrode materials or in medical application to name just a few.[46–48] Ahnfeldt *et al.*[49] have shown by a high-throughput synthesis in low molecular weight alcohols *e.g.* MeOH and EtOH that the synthesis of MIL-53 is, in principle, possible. These solvents have advantages such as low cost and ease of removal, making the synthesis of MIL-53 more sustainable. Although some studies have investigated the synthesis of MIL-53 in water and DMF,[45,50] a wide range of applied synthesis conditions *e.g.* temperature, reaction time, concentration, metal-to-linker ratio and additives make the direct comparison of these results complicated.[11,50–55] To the best of our knowledge, no reports of the successful synthesis and thorough characterisation of MIL-53 in simple alcohols have been reported previously. We present herein the MIL-53 synthesis in MeOH and EtOH to determine the influence of these solvents in comparison with MIL-53 synthesized in water and DMF. The MIL-53 aluminium derivative was used as the test compound due to its known lower toxicity in comparison with other derivatives such as chromium[16] and its commercial availability (as BasoliteA100®).

Experimental

Aluminium nitrate nonahydrate, $Al(NO_3)_3{\cdot}9H_2O$, and 1,4-benzenedicarboxylic acid (>98%) were purchased from Sigma Aldrich. *N*,*N*-Dimethylformamide, MeOH, EtOH and acetone were provided by Fisher-Scientific. All chemicals were used without further purifications. Deionised water (DI-water) was collected from a Millipore Direct-Q 5 UV water purification system.

Synthesis

MIL-53 was synthesized according to a modified synthesis protocol.[51] Briefly, a reaction mixture of $Al(NO_3)_3{\cdot}9H_2O$ (5.99 mmol; 2.246 g) and H_2BDC (5.38 mmol; 0.895 g) was prepared in 30 ml of solvent (DMF, water, MeOH or EtOH), stirred vigorously at room temperature for 15 min and transferred to a 45 ml Teflon-lined stainless steel autoclave. The reaction mixture was heated to 150 °C for 5 h after which the product was separated by centrifugation (4500 rpm for 30 min). The solution was decanted and the crystalline material washed with DMF (2 × 50 ml) and acetone (1 × 50 ml). The product, a white powder, was dried at 150 °C for 17 h. The unreacted starting material and residual solvent were removed from the as-synthesized samples (referred to as MIL53-AsSyn subsequently) by heating at 333 °C for 3 days (referred to as MIL53-Acti subsequently).[11] For simplification, the products are referred to as MIL-53(H_2O), MIL-53(DMF), MIL-53(MeOH) and MIL-53(EtOH), respectively.

Characterisation

X-Ray diffraction (XRD) measurement was performed using a PANanalytical X'Pert Pro diffractometer operated at 40 kV, 40 mA and Cu Kα radiation (λ = 1.540598 Å) equipped with a PIXCell3D detector. The experiments were conducted in continuous scanning mode with a goniometer fixed in the theta/theta orientation. For the incident beam site and detector site, a Soller slit of 0.04 rad and an incident beam mask of 15 mm were used. The imitated length was 10.0 mm. In a typical experiment, ~50 mg of MIL-53 powder was used and scans were conducted in the range of 5–35° 2θ with a step size of 0.006565° and a scan time of 51 s per step, resulting in a total measurement time of 17 min. For temperature-dependent XRD measurements, an AntonPaar HTK 1200 N oven was used. For all measurements, the sample was heated between 25 °C and 250 °C (between 25 °C and 200 °C in 25 °C steps with one additional measurement at 250 °C) and then cooled down to 25 °C. Additional diffractograms at 25 °C were measured immediately after reaching 25 °C again (0 min waiting time) and after waiting times of 30 min and 60 min, respectively. All the samples for the temperature-dependent XRD measurement were kept in a saturated water atmosphere for 3 days prior to XRD measurements. Scanning electron microscopy (SEM) was used to characterise the morphology and crystal size (from an average of 25 particles). Measurements were conducted with a JEOL JSM-7100F field emission gun (FEG) instrument with a beam voltage of 15 kV. The samples were sputtered with a 10 nm iridium film using a Quorum Q150T ES coater in order to increase the conductivity of the samples. Environmental SEM (ESEM) in varying relative humidity was performed using an FEI Quanta 650 ESEM at 15 kV. The samples were not coated for ESEM measurements. Thermal stability was investigated using a TA Instruments Q500 thermogravimetric analyser. The samples were heated up to 700 °C under air flow (100 ml min^{-1}) with a heating rate of 5 °C min^{-1}. The sample porosity and BET surface area were determined by N_2-adsoprtion *via* a Micromeritics Tristar II adsorber. Degassing of the samples was conducted under vacuum at 80 °C for 1 h and at 150 °C overnight. N_2-

Isotherms were measured at 77 K. The surface area was calculated by the BET method using 7 data points between 0.05 and 0.28 p/p_0. Water isotherms were measured with a Micromeritics 3Flex adsorber at 25 °C between 0.1 and 0.9 p/p_0. For a typical experiment, 100 mg of sample was degassed at 150 °C in a vacuum overnight prior to isotherm measurement. Water vapours of different relative humidities were created by bubbling dry dinitrogen through deionized water. For every data point, the maximum time allowed to reach equilibrium (pressure change not more than 5% for 600 s) was set to 16 h. FT-IR spectroscopy was performed on a Bruker Alpha equipped with a platinum ATR module. Spectra were measured with a 4 cm^{-1} resolution collecting 50 consecutive measurements.

Results and discussion

Investigation of morphology by SEM

SEM images of the powder samples synthesised using water, DMF and MeOH are shown in Fig. 1. When water is used as the solvent for synthesis, generating MIL-53(H_2O), micrometre-sized (~3 μm) star-shaped particles are observed (Fig. 1a and b), indicating intergrowth of orthorhombic crystals, the typical behaviour of MIL-53 single crystals.[56,57] After activation at high temperature, cracks and broken intergrown particles were observed (Fig. 1b), presumably caused by thermal stress during the activation process.

In contrast to particles prepared in water, the SEM images of MIL-53(DMF) reveal spherical particles with a size of 41 ± 17 nm, which agglomerate to form larger particles of several micrometres (see ESI† Fig. S2a). This can be partly explained by the drying process for SEM imaging, which caused strong particle agglomeration.[58] In contrast to the MIL-53(H_2O) samples, activation caused no cracks in the particles' surface (Fig. 1c), possibly as a result of the smaller particle size of MIL-53(DMF). Using MeOH as the solvent, two particle morphologies were observed: (1) spherical particles with a similar size to MIL-53(DMF) and (2) longer rod-shaped particles with comparable diameters to the spherical particles but with a substantially longer length of 178 ± 42 nm (Fig. 1d). As with MIL-53(DMF), a tendency towards agglomeration to micrometre-sized particles was observed (see Fig. S3a†). Interestingly, in DMF and MeOH, nanometre-sized particles are prepared.

Previous investigations to explain the different particle sizes observed for MIL-53 prepared in water or DMF have identified the varying deprotonation rate of the linker H_2BDC as the main reason for the behaviour in different solvents.[45] In these reactions, the reaction solvent acts as a base. In general, a faster nucleation rate is expected to lead to the formation of smaller particles.[59] A good indicator of basicity, and

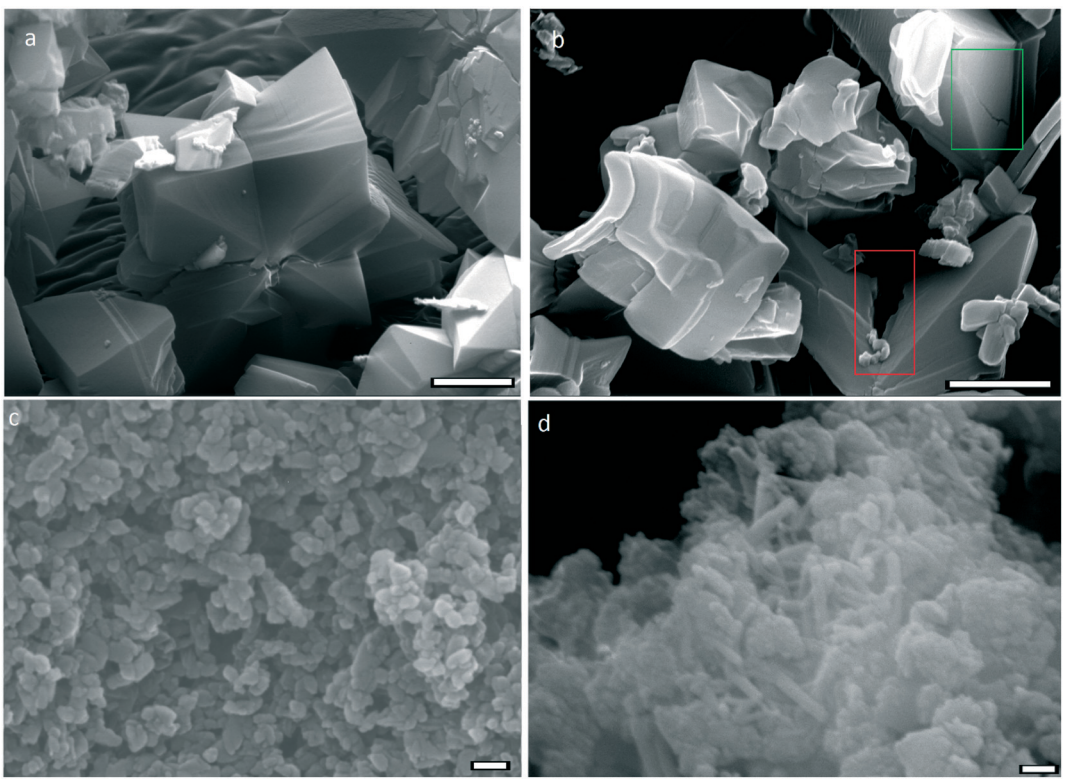

Fig. 1 Comparison of SEM images of the samples MIL-53(H_2O)-AsSyn (upper left, a), MIl-53(H_2O)-Acti (upper right, b), MIL-53(DMF)-Acti (lower left, c) and MIL-53(MeOH)-Acti (lower right, d). For the MIL-53(H_2O)-Acti sample, intergrown star-shaped particles are identified with a size of ~3000 nm. After activation by calcination, cracks (indicated by the green rectangle) and breaking of the intergrown crystals could be observed (red rectangle). Scale bar in a and b: 1 μm; scale bar in c and d: 100 nm.

in this regard of the deprotonation rate, is the p*K*a of the solvents used (water: 14;[60] DMF: −0.30,[61] MeOH = 15.7[61]). However, this measure suggests that MeOH is slightly more acidic than water and should, in principle, lead to the formation of larger particles. We therefore assume that the solubility of the linker in the reaction solvents also has a significant effect on the particle size during the formation of MIL-53. At a reaction temperature of 150 °C, the linker only dissolves partly in water (0.0065 g H_2BDC in 100 g water[62]) and reacts with metal ions to form MIL-53 seeds. We assume, due to the shape of MIL-53(H_2O) (see Fig. 1), that in water the growth from the already existing seeds is preferred over the nucleation of new seeds, which leads to the formation of particles with size exceeding several micrometres. In DMF (14.49 g H_2BDC in 100 g DMF[63]) and methanol (2.9 g H_2BDC in 100 g MeOH[61]), the solubility is several orders of magnitude higher in comparison with water. BDC^{2-} is therefore fully dissolved, leading to a greater number of seeds and hence more nanometre-sized MIL-53 particles. The solubility might affect the yield as well, whereas for DMF a nearly complete conversion was observed; the yields in methanol (52%) and water (18%) are significantly lower.

Investigation of the crystallinity and breathing effect of MIL-53 by XRD

The XRD patterns of the MIL-53 samples synthesised in water, DMF or MeOH before and after activation are shown in Fig. 2, including a comparison to the pattern calculated from the single crystal data.[11] Prior to activation, MIL-53(H_2O) has a pattern which is in good agreement with the calculated XRD pattern of MIL-53-AsSyn. During the synthesis, H_2BDC remains in the sample pores ensuring the large pore form. Due to interaction between H_2BDC and the pore walls, the pore diameter is slightly smaller (0.73 nm × 0.77 nm) in comparison with that of the activated large pore form[11] (0.85 nm × 0.85 nm), leading to a shift of the peaks in the XRD pattern (*e.g.* the peak in the calculated pattern at 2θ = 8.94° shifts to 8.72°). The activated MIL-53(H_2O) adsorbs water from ambient air, leading to shrinkage of the pores (0.26 nm × 1.36 nm). Both forms can be easily distinguished by XRD, where the large pore form shows a characteristic peak at ~15° while the small pore form is indicated by a peak at ~12°. The pattern of MIL-53(DMF)-AsSyn matches the calculated AsSyn pattern. The observed broader peaks are in agreement with the observed smaller particle size of MIL-53(DMF) in comparison with that of MIL-53(H_2O). After activation, these peaks were shifted to smaller 2θ values, showing the removal of H_2BDC. Similar intensities of the characteristic peaks at 12° and 15° may suggest equal proportions of small and large pores in the sample, respectively. In contrast to MIL-53(H_2O) and MIL-53(DMF), no peak at ~12° is observed in the pattern of MIL-53(MeOH) indicating the absence of the small pore form. The characteristic peaks are already in good agreement with the activated sample. Furthermore, the peak positions of MIL-53(MeOH) were not shifted to lower 2θ values after activation. This implies an activated MIL-53 sample.

The measurement of the internal pore surface area by BET helps to further confirm these assumptions. The measured

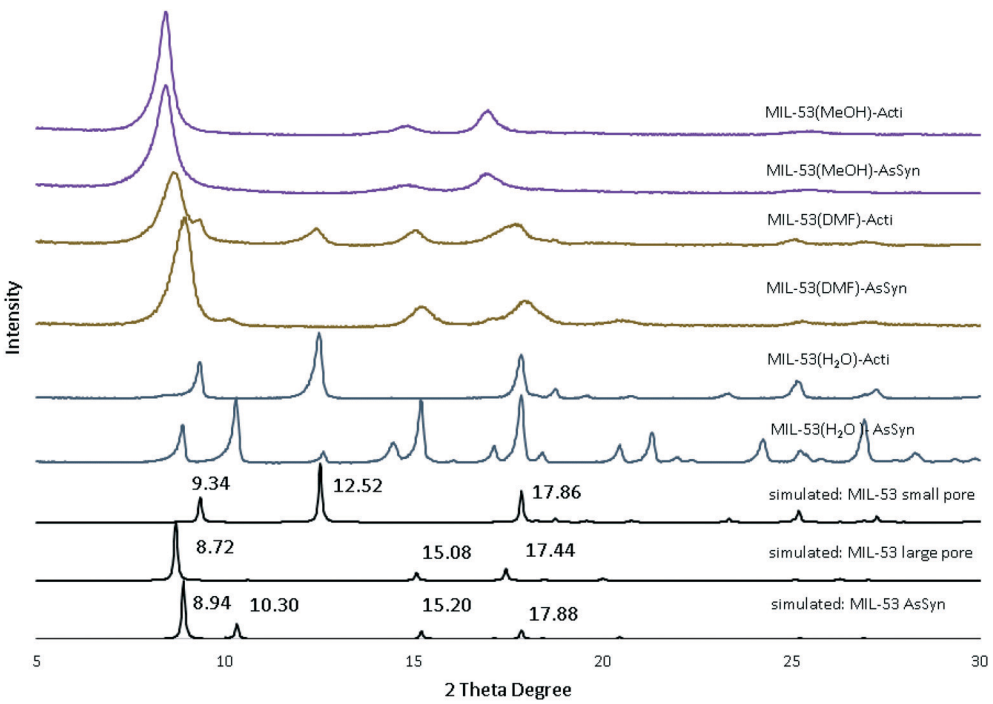

Fig. 2 XRD pattern of as-synthesized and activated MIL-53 synthesized in water, DMF and MeOH. For comparison, the XRD patterns of MIL-53-AsSyn containing H_2BDC, large and small pore forms of MIL-53 are simulated from the existing crystal data.[11]

BET surface areas of the activated samples of MIL-53(H_2O) and MIL-53(DMF) show the formation of porous, crystalline samples, with surface areas of 1002 $m^2 g^{-1}$ and 1084 $m^2 g^{-1}$, respectively, in good agreement with previously reported data.[11,21] The measured BET surface area of MIL-53(MeOH)-Acti (895 $m^2 g^{-1}$) is slightly lower than those the samples prepared in water and DMF. However, in the case of MIL-53(MeOH), only a small difference between the as-synthesized sample and the activated sample regarding the surface area and microporosity (~10% for both) was observed (see Table 1). For MIL-53(DMF), the differences in surface area (~29%) and microporosity (~49%) are larger and, for MIL-53(H_2O)-AsSyn, no porosity could be measured. This may indicate, combined with the results of the XRD measurements, that minimal H_2BDC is trapped in MIL-53(MeOH) after the reaction, and milder or even no activation might be necessary to achieve the framework porosity. The MIL-53 derivative synthesised using EtOH as the solvent revealed a similar particle size and morphology to MIL-53(MeOH) (see Fig. S5†). The characteristic peaks in XRD at 2θ = 8.48°, 15.20° and 17.34° indicate the synthesis of MIL-53 (see Fig. S6†). However, the greatly reduced intensity in comparison with the samples prepared in water, DMF and MeOH implies the synthesis of a sample with low crystallinity, verifying the observation of Ahnfeldt *et al.*[18] Furthermore, after activation, the characteristic diffraction peaks were no longer observed, and an amorphous product was obtained. Therefore, no further investigation of MIL-53(EtOH) was conducted in this research.

Investigation of the breathing effect and water adsorption kinetics

As already mentioned, the XRD pattern of MIL-53 helps to distinguish between the small and large pore forms. The comparison between the AsSyn and activated samples of MIL-53 implies different water adsorption kinetics and breathing phenomena depending on the solvent used for the synthesis. To further investigate this observation, temperature-dependent PXRD was conducted. The samples were saturated in water vapour and the XRD pattern was measured at different temperatures to investigate the removal of water from the pores and consequently the breathing phenomenon. Fig. 3a shows the temperature-dependent XRD pattern of MIL-53(H_2O)-Acti. Only a peak at $2\theta \sim 12°$ is visible at 25 °C and the sample is found to be solely in the small pore form. At approximately 75 °C, the small pore peak becomes broader and decreases in intensity, while the large pore peak at 15° increases in intensity. At 150 °C, only the large pore form was observed. After cooling down to 25 °C again, the intensity of the small pore peak at 12° increased, whereas the intensity of the large pore peak at 15° decreased with every consecutive waiting step, showing fast water adsorption from ambient air.

As shown in Fig. 3b, the structure of the MIL-53(DMF) sample did not change completely into the small pore form after being exposed to a saturated water atmosphere. Instead, the XRD pattern indicates a 1:1 ratio of the large pore to small pore based on the peak intensities. During heating, the small pore peak at 12.51° shifts to larger 2θ values when the temperature was increased from 25 °C to 100 °C with a shift of up to 0.64°. At higher temperature, this peak shifts back to the initial position with a reduction in intensity until the loss of the peak at 200 °C. After cooling down the sample back to 25 °C, a small peak at 12.49° appeared after a 1 h period. This and the 1:1 ratio between the small and large pore forms in the starting material suggest slower water adsorption in comparison with the MIL-53(H_2O) sample. In contrast, in the XRD pattern of MIL-53(MeOH)-Acti (Fig. 3c), the small pore peak at 2θ = ~12° could not be observed, which implies that MIL-53(MeOH) does not show any breathing phenomenon at all. For the initial measurement at 25 °C, the observed peaks were considerably lower in intensity than those for MIL-53(H_2O)-Acti and MIL-53(DMF)-Acti. In order to understand this effect, environmental SEM (ESEM) measurements were employed. At higher humidity levels (>80%), the particles start to fuse (see Fig. 4), which might lead to a lower crystallinity of the sample; a phenomena not observed for MIL-53(DMF) which has a similar morphology (see Fig. 5). However, the temperature-dependent SEM shows that, in contrast to moisture-sensitive MOFs like HKUST-1 or MOF-5,[32] the crystallinity of MIL-53(MeOH) is restored after the removal of water.

The measured FTIR spectra of the activated sample further confirm this observation (see Fig. S7†). The MIL-53 samples were dried at 125 °C and the IR spectra measured 5 min after removal from the oven. The IR spectra of all the samples show peaks at 1414 cm^{-1} and 1510 cm^{-1}, which are attributed to the symmetrical and asymmetrical stretching vibrations of the framework carboxylate groups.[64] The peaks at 1120 cm^{-1}, 3463 cm^{-1} and 3610 cm^{-1} are only observed in the IR spectrum of MIL-53(H_2O), which indicate the adsorption

Table 1 Comparison of the BET surface area and microporosity of the prepared MIL-53 samples before and after activation. For MIL-53(H_2O)-AsSyn, no porosity could be measured

Compound	BET surface area ($m^2 g^{-1}$)	*t*-Plot micropore volume ($cm^3 g^{-1}$)
MIL-53(H_2O)-AsSyn	—	—
MIL-53(H_2O)-Acti	1002	0.44
MIL-53(DMF)-AsSyn	767	0.23
MIL-53(DMF)-Acti	1084	0.45
MIL-53(MeOH)-AsSyn	805	0.35
MIL-53(MeOH)-Acti	895	0.39

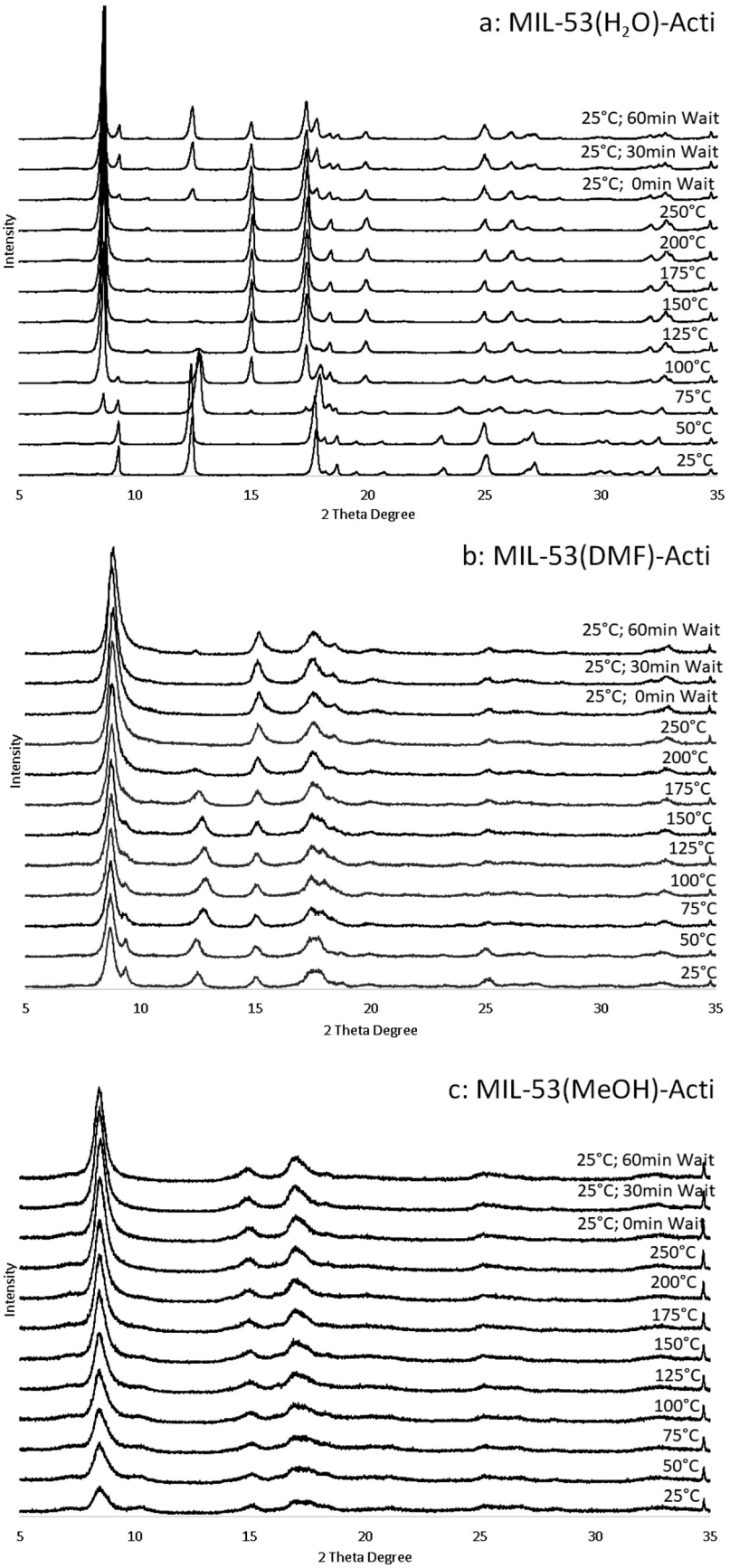

Fig. 3 XRD patterns of a) MIL-53(H_2O)-Acti, b) MIL-53(DMF)-Acti and c) MIL-53(MeOH)-Acti measured at varying temperatures. All the samples were saturated with water before the series of XRD measurements.

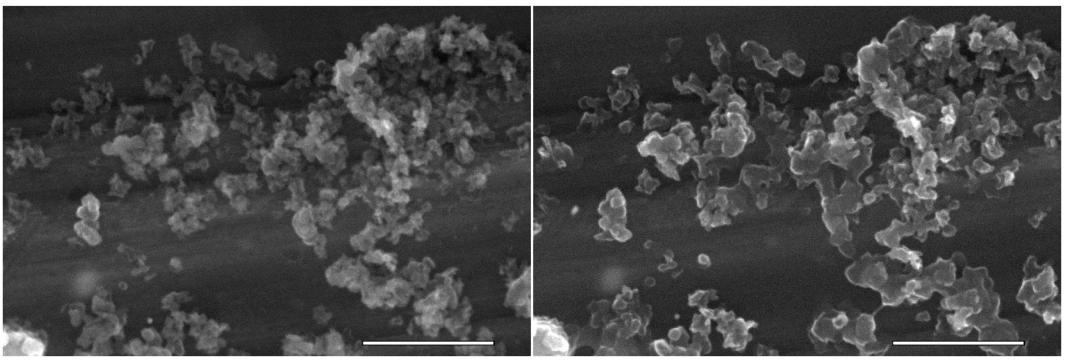

Fig. 4 Environmental SEM images of MIL-53(MeOH)-Acti at 60% relative humidity (left) and 80% relative humidity (right). Particles start to fuse at higher humidity levels. Scale bar: 2 μm.

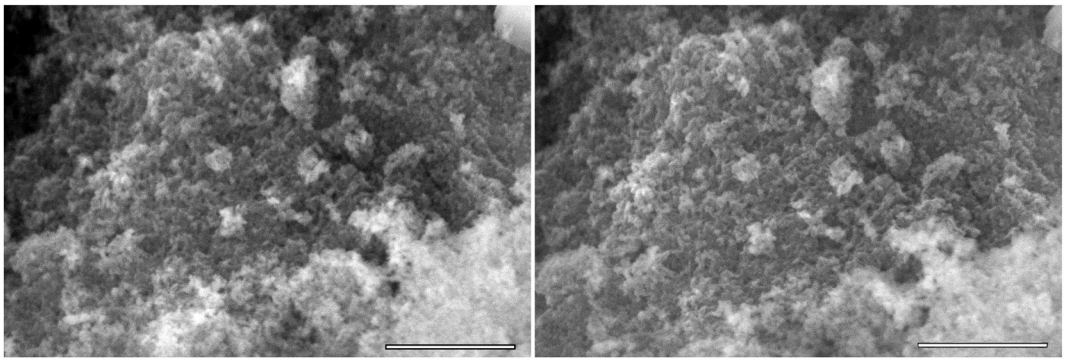

Fig. 5 Environmental SEM images of MIL-53(DMF)-Acti at 60% relative humidity (left) and 80% relative humidity (right). No change in the particles was observed. Scale bar: 2 μm.

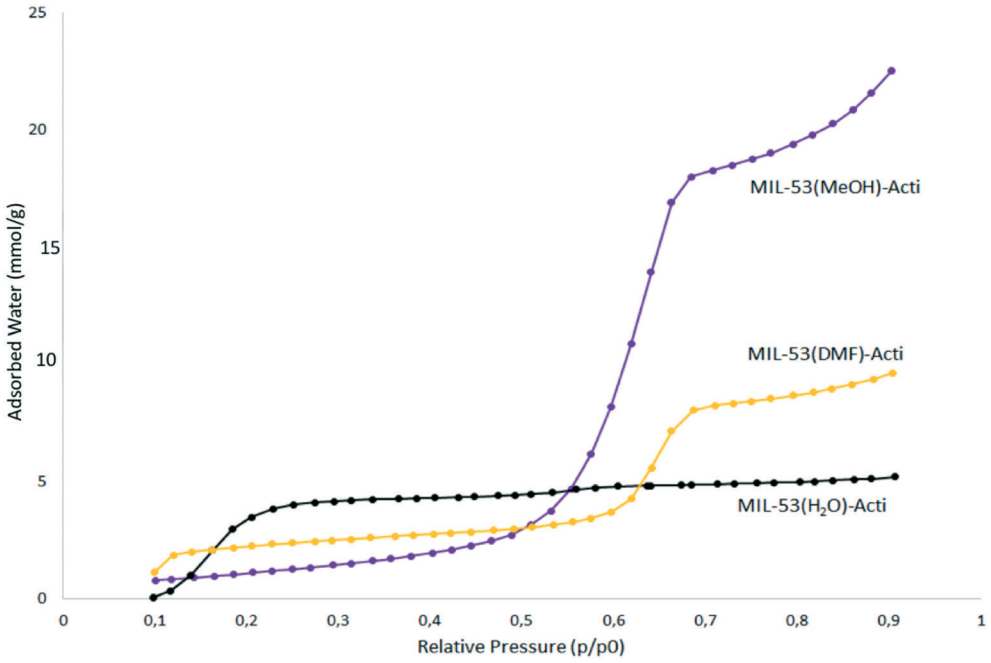

Fig. 6 Water isotherm of MIL-53(H_2O)-Acti (black), MIL-53(DMF)-Acti (yellow) and MIL-53(MeOH)-Acti (purple) measured at 25 °C and ambient pressure. The isotherms were measured between 0.1 and 0.9 p/p_0.

of water. Fig. 6 shows the water isotherms for the activated samples MIL-53(H_2O), MIL-53(DMF) and MIL-53(MeOH) which verify the different hydrophobicities of the samples. The MIL-53 derivative prepared in water shows a fast uptake of water at a low relative pressure of 0.1 p/p_0 reaching a plateau at 5 mmol g^{-1} adsorbed water. The isotherm has a type-I

isotherm shape. This implies a strong interaction between the adsorbate and adsorbent at low relative pressure and that the sample does not exhibit macroporosity. The pores contract into the small pore form, preventing further water adsorption. At lower relative pressure, both MIL-53(DMF) and MIL-53(MeOH) show only a low water uptake followed by a sharp increase at 0.6 p/p_0 for MIL-53(DMF) and at 0.5 p/p_0 for MIL-53(MeOH). The behaviour is maintained at higher relative pressure. At 0.9 p/p_0 for MIL-53(DMF), a total uptake of 10 mmol g^{-1} was measured while the total uptake of MIL-53(MeOH) is 22 mmol g^{-1}. For both samples, the profiles resemble a type-V isotherm, which indicates a weak interaction at low relative pressure followed by clustering of water molecules (pore condensation) at higher relative pressure. Above 0.8 p/p_0, a further increase of water uptake indicates interparticle water adsorption.

Similar trends for water adsorption for the MIL-53 samples were already observed. Mounfield and Walton[50] confirmed the dependency between the reaction temperature and breathing phenomenon for MIL-53(DMF). MIL-53(DMF) prepared at 120 °C does not show any breathing phenomena while the 220 °C sample shows a small breathing effect. Furthermore, at low relative water pressure (<0.5 p/p_0), the samples show lower water uptake (1.5 mmol g^{-1} for the DMF samples in comparison with 4 mmol g^{-1} for MIL-56(H_2O)[50]). The increased hydrophobicity was attributed to the remaining DMF molecules in the framework. In this study, activation was conducted at elevated temperature to ensure the complete removal of any residue and TGA measurements (see Fig. S8†) have verified the absence of DMF in the activated samples. The absence of weight loss steps between 100 °C and 250 °C (residue of DMF[50]) or 275 °C and 420 °C (residue of H_2BDC[11]) indicates the formation of a product free of any residual species in the pores of the activated species. The MIL-53(MeOH) sample prior to activation includes DMF (see Fig. S8†) but this is introduced during the washing step, suggesting that any residual unreacted H_2BDC can be readily removed from the MIL-53(MeOH) sample. Interestingly, the thermal stability of MIL-53(DMF) and MIL-53(MeOH) (~460 °C) was slightly reduced in comparison with that of MIL-53(H_2O) (~500 °C). This may be due to the smaller particle size of MIL-53(MeOH) and MIL-53(DMF) in comparison with that of MIL-53(H_2O). Even so, the thermal stability of MIL-53 prepared in DMF or MeOH is higher in comparison with that of other commercially available carboxylate-containing MOFs like HKUST-1 (240 °C[65]) or MOF-177 (400 °C[66]). Therefore, the varying hydrophobicities and breathing effects seem to be an intrinsic characteristic of the MIL-53 derivatives and can be controlled by the usage of different solvents. As a side note, MIL-53(DMF) seems to have an even higher hydrophobicity than MIL-53(MeOH) (increase of water uptake at 0.6 p/p_0 in comparison with 0.5 p/p_0 in the water isotherms) but decomposes at high humidity. After measurement of the water isotherm, the porosity of MIL-53(DMF) (see Fig. S12†) (BET area: 1084 m^2 g^{-1} → 377 m^2 g^{-1}) is greatly reduced, while only a small difference of ~4% for MIL-53(MeOH) (895 m^2 g^{-1} → 862 m^2 g^{-1}) was observed. The porosity of MIL-53(H_2O) even slightly increased from 1002 m^2 g^{-1} to 1021 m^2 g^{-1} (see Table S15†).

Conclusion

We have successfully prepared MIL-53 in the low molecular weight alcohol MeOH employing a reaction temperature of 150 °C, lower than that typically used for analogous water or DMF-based reactions. This leads to the formation of a sample with nano-sized particles and comparable properties with MIL-53 prepared in water and DMF. The sample prepared in MeOH shows a high porosity and thermal stability, which is typical for the MIL-53 class. In DMF and MeOH, the solubility of H_2BDC at the reaction temperature is several orders of magnitude higher in comparison with that in water, which leads to faster nucleation and crystal growth. This results in the formation of nanometer-sized particles. Further, MIL-53(MeOH) does not show any breathing effects, which can be partly attributed to the increased hydrophobicity of the sample. Interestingly, the MIL-53(MeOH) particles have a tendency to fuse at high humidity. However, in contrast to moisture-sensitive MOFs like MOF-5, the framework of MIL-53(MeOH) does not collapse and the crystallinity of MIL-53(MeOH) is restored after removal of water. Furthermore, the measurement of the internal surface area confirmed the synthesis of highly porous MIL-53(MeOH) with minimal activation required. Further research has to be done to understand why the formation of MIL-53 was possible in MeOH but not in EtOH despite similar chemical properties of both solvents.

Conflicts of interest

There are no conflicts to declare.

Acknowledgements

This work was supported by the Engineering and Physical Sciences Research Council (EPSRC, EP/L022494/1). JW gratefully acknowledges receipt of a University of Nottingham Research Scholarship. The authors thank the Nanoscale and Microscale Centre (nmRC) for providing access to instrumentation and Ms. Nicola J. Weston for assistance with ESEM. Furthermore, the authors thank Prof. Dr. Michael Wark and Sven Warfsmann (Technical Chemistry, Institute for Chemistry, Carl-von-Ossietzky Universität Oldenburg) for measurement of N_2 and water isotherms.

References

1 R. Ricco, C. Pfeiffer, K. Sumida, C. J. Sumby, P. Falcaro, S. Furukawa, N. R. Champness and C. J. Doonan, *CrystEngComm*, 2016, **18**, 6532–6542.
2 J.-R. Li, R. J. Kuppler and H.-C. Zhou, *Chem. Soc. Rev.*, 2009, **38**, 1477–1504.
3 R. C. Huxford, J. Della Rocca and W. Lin, *Curr. Opin. Chem. Biol.*, 2010, **14**, 262–268.

4 X. Lian, Y. Fang, E. Joseph, Q. Wang, J. Li, S. Banerjee, C. Lollar, X. Wang and H.-C. Zhou, *Chem. Soc. Rev.*, 2017, **46**, 3386–3401.
5 W. M. Bloch, N. R. Champness and C. J. Doonan, *Angew. Chem., Int. Ed.*, 2015, **54**, 12860–12867.
6 V. Stavila, A. A. Talin and M. D. Allendorf, *Chem. Soc. Rev.*, 2014, **43**, 5994–6010.
7 R. Ricco, L. Malfatti, M. Takahashi, A. J. Hill and P. Falcaro, *J. Mater. Chem. A*, 2013, **1**, 13033.
8 G. Férey, M. Latroche, C. Serre, F. Millange, T. Loiseau and A. Percheron-Guégan, *Chem. Commun.*, 2003, 2976–2977.
9 T. Devic, F. Salles, S. Bourrelly, B. Moulin, G. Maurin, P. Horcajada, C. Serre, A. Vimont, J.-C. Lavalley, H. Leclerc, G. Clet, M. Daturi, P. L. Llewellyn, Y. Filinchuk and G. Férey, *J. Mater. Chem.*, 2012, **22**, 10266.
10 F. Millange, N. Guillou, R. I. Walton, J.-M. Greneche, I. Margiolaki and G. Ferey, *Chem. Commun.*, 2008, 4732–4734.
11 T. Loiseau, C. Serre, C. Huguenard, G. Fink, F. Taulelle, M. Henry, T. Bataille and G. Ferey, *Chem. – Eur. J.*, 2004, **10**, 1373–1382.
12 C. Volkringer, T. Loiseau, N. Guillou, G. Ferey, E. Elkaim and A. Vimont, *Dalton Trans.*, 2009, 2241–2249.
13 J. P. S. Mowat, S. R. Miller, A. M. Z. Slawin, V. R. Seymour, S. E. Ashbrook and P. A. Wright, *Microporous Mesoporous Mater.*, 2011, **142**, 322–333.
14 J. Gascon, U. Aktay, M. Hernandez-Alonso, G. van Klink and F. Kapteijn, *J. Catal.*, 2009, **261**, 75–87.
15 L. Liu, X. Wang and A. J. Jacobson, *Dalton Trans.*, 2010, **39**, 1722–1725.
16 S. Biswas, T. Ahnfeldt and N. Stock, *Inorg. Chem.*, 2011, **50**, 9518–9526.
17 J. Wack, R. Siegel, T. Ahnfeldt, N. Stock, L. Mafra and J. Senker, *J. Phys. Chem. C*, 2013, **117**, 19991–20001.
18 T. Ahnfeldt, D. Gunzelmann, T. Loiseau, D. Hirsemann, J. Senker, G. Ferey and N. Stock, *Inorg. Chem.*, 2009, **48**, 3057–3064.
19 M. Mendt, B. Jee, N. Stock, T. Ahnfeldt, M. Hartmann, D. Himsl and A. Pöppl, *J. Phys. Chem. C*, 2010, **114**, 19443–19451.
20 J. Yang, X. Yan, T. Xue and Y. Liu, *RSC Adv.*, 2016, **6**, 55266–55271.
21 S. Pourebrahimi, M. Kazemeini, E. Ganji Babakhani and A. Taheri, *Microporous Mesoporous Mater.*, 2015, **218**, 144–152.
22 K. Akhbari and A. Morsali, *Mater. Lett.*, 2015, **141**, 315–318.
23 T. A. Vu, G. H. Le, C. D. Dao, L. Q. Dang, K. T. Nguyen, Q. K. Nguyen, P. T. Dang, H. T. K. Tran, Q. T. Duong, T. V. Nguyen and G. D. Lee, *RSC Adv.*, 2015, **5**, 5261–5268.
24 J. Yan, S. Jiang, S. Ji, D. Shi and H. Cheng, *Sci. China: Chem.*, 2015, **58**, 1544–1552.
25 U. Ravon, G. Chaplais, C. Chizallet, B. Seyyedi, F. Bonino, S. Bordiga, N. Bats and D. Farrusseng, *ChemCatChem*, 2010, **2**, 1235–1238.
26 P. Horcajada, T. Chalati, C. Serre, B. Gillet, C. Sebrie, T. Baati, J. F. Eubank, D. Heurtaux, P. Clayette, C. Kreuz, J.-S. Chang, Y. K. Hwang, V. Marsaud, P.-N. Bories, L. Cynober, S. Gil, G. Ferey, P. Couvreur and R. Gref, *Nat. Mater.*, 2010, **9**, 172–178.
27 C.-X. Yang, H.-B. Ren and X.-P. Yan, *Anal. Chem.*, 2013, **85**, 7441–7446.
28 L. Paseta, E. Simón-Gaudó, F. Gracia-Gorría and J. Coronas, *Chem. Eng. J.*, 2016, **292**, 28–34.
29 M. Alhamami, H. Doan and C.-H. Cheng, *Materials*, 2014, **7**, 3198–3250.
30 A. Schneemann, V. Bon, I. Schwedler, I. Senkovska, S. Kaskel and R. A. Fischer, *Chem. Soc. Rev.*, 2014, **43**, 6062–6096.
31 F. Millange, N. Guillou, M. E. Medina, G. Férey, A. Carlin-Sinclair, K. M. Golden and R. I. Walton, *Chem. Mater.*, 2010, **22**, 4237–4245.
32 J. Canivet, A. Fateeva, Y. Guo, B. Coasne and D. Farrusseng, *Chem. Soc. Rev.*, 2014, **43**, 5594–5617.
33 J. Liu, F. Zhang, X. Zou, G. Yu, N. Zhao, S. Fan and G. Zhu, *Chem. Commun.*, 2013, **49**, 7430–7432.
34 H. Kim, S. Yang, S. R. Rao, S. Narayanan, E. A. Kapustin, H. Furukawa, A. S. Umans, O. M. Yaghi and E. N. Wang, *Science*, 2017, **256**, 430–434.
35 C. Janiak and S. K. Henninger, *Chimia*, 2013, **67**, 419–424.
36 S. Biswas, T. Remy, S. Couck, D. Denysenko, G. Rampelberg, J. F. M. Denayer, D. Volkmer, C. Detavernier and P. van der Voort, *Phys. Chem. Chem. Phys.*, 2013, **15**, 3552–3561.
37 A. Laybourn, J. Katrib, R. S. Ferrari-John, C. G. Morris, S. Yang, O. Udoudo, T. L. Easun, C. Dodds, N. R. Champness, S. W. Kingman and M. Schröder, *J. Mater. Chem. A*, 2017, **5**, 7333–7338.
38 E. Haque, N. A. Khan, J. H. Park and S. H. Jhung, *Chemistry*, 2010, **16**, 1046–1052.
39 P. A. Bayliss, I. A. Ibarra, E. Pérez, S. Yang, C. C. Tang, M. Poliakoff and M. Schröder, *Green Chem.*, 2014, **16**, 3796.
40 N. Stock and S. Biswas, *Chem. Rev.*, 2012, **112**, 933–969.
41 C. A. Redlich, W. S. Beckett, J. Sparer, K. W. Barwick, C. A. Riely, H. Miller, S. L. Sigal, S. L. Shalat and M. R. Cullen, *Ann. Intern. Med.*, 1988, **108**, 680–686.
42 W. M. Haynes, *CRC handbook of Chemistry and Physics, (2016) 96th Edition*, Boca Raton, 2016.
43 E. Tynan, P. Jensen, P. E. Kruger and A. C. Lees, *Chem. Commun.*, 2004, 776–777.
44 D. Prat, O. Pardigon, H.-W. Flemming, S. Letestu, V. Ducandas, P. Isnard, E. Guntrum, T. Senac, S. Ruisseau, P. Cruciani and P. Hosek, *Org. Process Res. Dev.*, 2013, **17**, 1517–1525.
45 X. Cheng, A. Zhang, K. Hou, M. Liu, Y. Wang, C. Song, G. Zhang and X. Guo, *Dalton Trans.*, 2013, **42**, 13698–13705.
46 W. Lin, W. J. Rieter and K. M. L. Taylor, *Angew. Chem., Int. Ed.*, 2009, **48**, 650–658.
47 M. Sindoro, N. Yanai, A.-Y. Jee and S. Granick, *Acc. Chem. Res.*, 2014, **47**, 459–469.
48 A. Majedi, F. Davar and A. R. Abbasi, *Int. J. Nano Dimens.*, 2016, **7**, 1–14.
49 T. Ahnfeldt, N. Guillou, D. Gunzelmann, I. Margiolaki, T. Loiseau, G. Ferey, J. Senker and N. Stock, *Angew. Chem., Int. Ed.*, 2009, **48**, 5163–5166.
50 W. P. Mounfield III and K. S. Walton, *J. Colloid Interface Sci.*, 2015, **447**, 33–39.
51 H. Fan, H. Xia, C. Kong and L. Chen, *Int. J. Hydrogen Energy*, 2013, **38**, 10795–10801.

52 C. Scherb, A. Schödel and T. Bein, *Angew. Chem.*, 2008, **120**, 5861–5863.
53 L. Alaerts, M. Maes, L. Giebeler, P. A. Jacobs, J. A. Martens, J. F. M. Denayer, C. E. A. Kirschhock and D. E. de Vos, *J. Am. Chem. Soc.*, 2008, **130**, 14170–14178.
54 T. K. Trung, P. Trens, N. Tanchoux, S. Bourrelly, P. L. Llewellyn, S. Loera-Serna, C. Serre, T. Loiseau, F. Fajula and G. Ferey, *J. Am. Chem. Soc.*, 2008, **130**, 16926–16932.
55 M. Sánchez-Sánchez, N. Getachew, K. Díaz, M. Díaz-García, Y. Chebudeb and I. Díaza, *Green Chem.*, 2015, **17**, 1500–1509.
56 F. Zhang, X. Zou, F. Sun, H. Ren, Y. Jiang and G. Zhu, *CrystEngComm*, 2012, **14**, 5487–5492.
57 X. Qian, Z. Zhong, B. Yadian, J. Wu, K. Zhou, J. S.-k. Teo, L. Chen, Y. Long and Y. Huang, *Int. J. Hydrogen Energy*, 2014, **39**, 14496–14502.
58 S. Sorribas, B. Zornoza, P. Serra-Crespo, J. Gascon, F. Kapteijn, C. Téllez and J. Coronas, *Microporous Mesoporous Mater.*, 2016, **225**, 116–121.
59 *Handbook of Industrial Crystallization*, Butterworth-Heinemann, Boston, ed. A. S. Myerson, 2nd edn, 2002.
60 R. C. Dougherty and L. N. Howard, *J. Chem. Phys.*, 1988, **109**, 7379–7393.
61 D. D. Perrin, *Dissociation Constants of Organic Acids and Bases*, Butterworths, London, 1965.
62 A. Apelblat, E. Manzurola and N. Abo Balal, *J. Chem. Phys.*, 2006, **38**, 565–571.
63 P. Ma and M. Chen, *J. Chem. Eng. Data*, 2003, **11**, 334–337.
64 J. M. Salazar, G. Weber, J. M. Simon, I. Bezverkhyy and J. P. Bellat, *J. Chem. Phys.*, 2015, **142**, 124702.
65 S. S.-Y. Chui, S. M.-F. Lo, J. P. H. Charmant, A. G. Orpen and I. D. Williams, *Science*, 1999, **283**, 1148–1150.
66 D. Saha and S. Deng, *J. Phys. Chem. Lett.*, 2010, **1**, 73–78.